Inorganic Chemistry

pubs.acs.org/IC Article

Probing the Mechanism for 2,4′-Dihydroxyacetophenone Dioxygenase Using Biomimetic Iron Complexes

Atanu Banerjee, Jia Li, Monika A. Molenda, Adedamola A. Opalade, Amitava Adhikary, William W. Brennessel, Aramice Y. S. Malkhasian, Timothy A. Jackson, and Ferman A. Chavez*

Cite This: *Inorg. Chem.* 2021, 60, 7168−7179

ABSTRACT: In this study, we report the synthesis and characterization of [Fe(T1Et4iPrIP)(2-OH-AP)(OTf)](OTf) (**2**), [Fe(T1Et4iPrIP)(2-O-AP)](OTf) (**3**), and [Fe(T1Et4iPrIP)(DMF)$_3$](OTf)$_3$ (**4**) (T1Et4iPrIP = tris(1-ethyl-4-isopropyl-imidazolyl)phosphine; 2-OH-AP = 2-hydroxyacetophenone, and 2-O-AP$^-$ = monodeprotonated 2-hydroxyacetophenone). Both **2** and **3** serve as model complexes for the enzyme−substrate adduct for the nonheme enzyme 2,4′-dihydroacetophenone (DHAP) dioxygenase or DAD, while **4** serves as a model for the ferric form of DAD. Complexes **2**−**4** have been characterized by X-ray crystallography which reveals T1Et4iPrIP to bind iron in a tridentate fashion. Complex **2** additionally contains a bidentate 2-OH-AP ligand and a monodentate triflate ligand yielding distorted octahedral geometry, while **3** possesses a bidentate 2-O-AP$^-$ ligand and exhibits distorted trigonal bipyramidal geometry (τ = 0.56). Complex **4** displays distorted octahedral geometry with 3 DMF ligands completing the ligand set. The UV−vis spectrum of **2** matches more closely to the DAD-substrate spectrum than **3**, and therefore, it is believed that the substrate for DAD is bound in the protonated form. TD-DFT studies indicate that visible absorption bands for **2** and **3** are due to MLCT bands. Complexes **2** and **3** are capable of oxidizing the coordinated substrate mimics in a stoichiometric and catalytic fashion in the presence of O$_2$. Complex **4** does not convert 2-OH-AP to products under the same catalytic conditions; however, it becomes anaerobically reduced in the presence of 2 equiv 2-OH-AP to **2**.

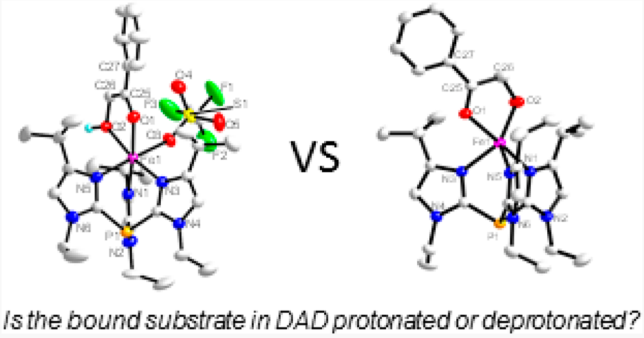

■ INTRODUCTION

The compound Bisphenol A is catabolized by various bacteria.[1] Formation of 2,4′-dihydroxyacetophenone (DHAP, Scheme 1) is located at a dead-end in the metabolic pathway, and builds up.[2] *Alcaligenes* sp. was found to utilize DHAP as a substrate.[3] In these bacteria, DHAP dioxygenase (DAD) in the presence of oxygen cleaves DHAP to yield 4-hydroxybenzoic acid and formic acid (Scheme 1).[4]

Scheme 1. Reaction Catalyzed for 2,4′-Dihydroxyacetophenone (DHAP) Dioxygenase (DAD)

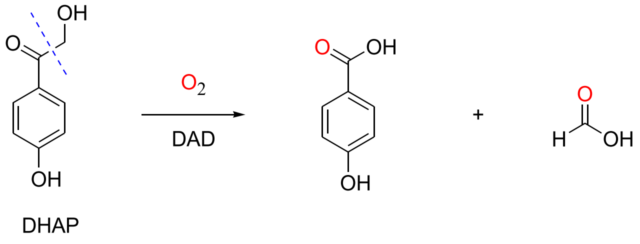

DAD's mechanism of action is unlike that of any known dioxygenase.[5] Other dioxygenases introduce two atoms of molecular O$_2$ while cleaving the aromatic ring;[1,6,7] DAD introduces two oxygen atoms from molecular O$_2$ into 2,4′-dihydroxyacetophenone with cleavage at the side chain.[8,9] The X-ray structure of DAD was initially determined by Cooper and co-workers.[10] The structure features iron(II) coordinated to three histidine nitrogens. After obtaining a structure at higher resolution, the additional ligand was determined to be an acetate molecule bonded in a monodentate fashion.[11,12]

Although DAD was isolated as mostly in the ferrous form, 6−8% of the enzyme was present as high-spin iron(III).[10] A modified mechanism first proposed by Enya et al. involves initial isomerization of DHAP to the *cis*-1,2-ethenediol form (Scheme 2, **I**) prior to interaction with the iron(III) active site

Received: January 26, 2021
Published: April 26, 2021

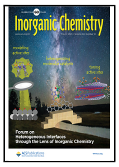

https://doi.org/10.1021/acs.inorgchem.1c00167
Inorg. Chem. 2021, 60, 7168−7179

Scheme 2. Mechanism for DAD Proposed by Enya et al.[1]

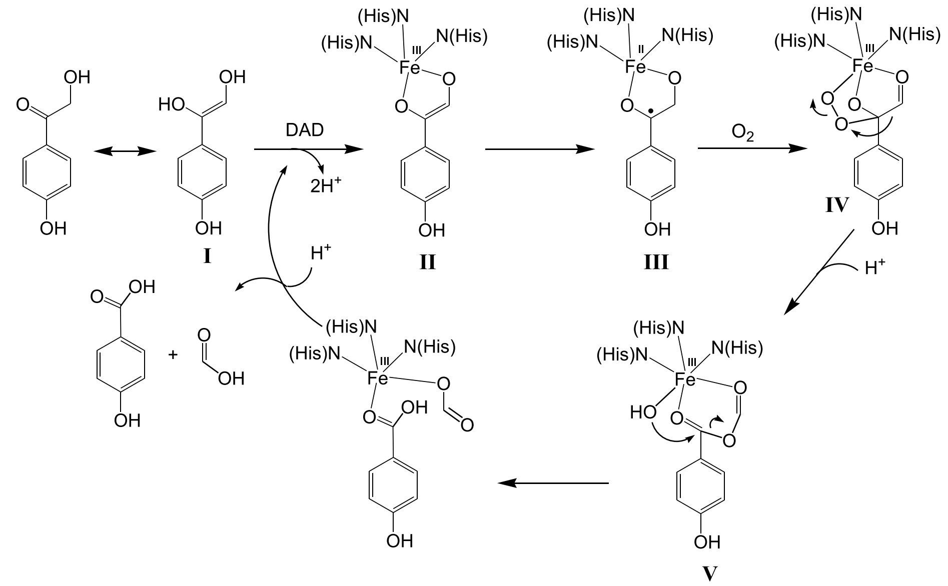

of the enzyme.[1] Anaerobic UV−vis studies suggest that DHAP first binds to iron(III) (Scheme 2, **II**) and subsequently transfers an electron to the iron center, reducing it to iron(II) with concomitant formation of a radical on the substrate (Scheme 2, **III**). Reaction with O_2 results in binding of the oxygen molecule to both the iron and organic moiety yielding an alkylperoxide intermediate (Scheme 2, **IV**). This mechanism is similar to intradiol catechol-1,2-dioxygenase.[13] Migration of the 4-hydroxybenzoyl group to form acid anhydride (Scheme 2, **V**) followed by hydrolytic cleavage yields 4-hydroxybenzoic and formic acid. It should be noted that this mechanism has been challenged.[14−16]

Model Studies. Investigators have modeled the DAD reaction using a trispyrazolylborate-Fe(II) complex.[7,15,17] The complex reacts with O_2 in benzene at 10 °C. It was also determined that the presence of the C−H bond in the CH_2O^- portion of the substrate was critical. Based on further radical scavenging studies, it was concluded that H atom abstraction of the C−H group adjacent to the alkoxide by an iron(III)-superoxo species occurs yielding Fe^{III}−OOH. This may convert to a dioxetane ring as proposed by Siewert et al.[18] Heterolytic cleavage of the alkylhydroperoxide or the dioxetane species would result in formation of 2 equiv carboxylic acid.

The optical absorption of the ferric form of DAD from *Burkholderia* sp. strain AZ11 (350 nm (5800 M^{-1} cm^{-1}) and 560 nm (1400 M^{-1} cm^{-1})) indicates that charge transfer bands dominate the spectrum.[1,7] The nature of these bands to our knowledge have not been addressed. When the substrate is added to the enzyme under nitrogen, an absorption band at 400 nm is observed. The authors suggest that this could result from substrate coordination to the iron(III) active site.[1] In the catalytic process, both forms of DAD, ferrous and ferric, would have to be cycled to effect turnover.

As pointed out by Zhang et al., although mechanisms for DAD have been put forward, evidence for proposed intermediates have yet to be confirmed experimentally.[14] Model complexes employed by Paine and co-workers contains iron coordinated to an anionic ligand with pyrazolyl donors rather than neutral imidazolyl donors.[15] To address this difference, we have sought to employ a tris-imidazolyl donor set to more accurately mimic the DAD iron coordination site. Furthermore, although it has been assumed in biomimetic studies that DAD catalyzes the turnover of 2,4′-HAP as a monoanion, there is no evidence that this is the mode of binding as suggested by Zhang et al.[14] To address these issues and elucidate intermediate species, we have employed tris(1-ethyl-4-isopropyl-imidazolyl)phosphine (T1Et4iPrIP, Scheme 3) as our tris-histidinyl mimic and have synthesized, biomimetic enzyme−substrate adducts for the protonated ($[Fe^{II}(T1Et4iPrIP)(2\text{-}OH\text{-}AP)(OTf)](OTf)$; 2-OH-AP = 2-hydroxyacetophenone) and the deprotonated form of the substrate ($[Fe^{II}(T1Et4iPrIP)(2\text{-}O\text{-}AP)](OTf)$; 2-O-$AP^-$ = monodeprotonated 2-hydroxyacetophenone). Furthermore, we have synthesized the ferric complex ($[Fe^{III}(T1Et4iPrIP)(DMF)_3](OTf)_3$) to compare the spectroscopy and reactivity with the ferrous forms.

Scheme 3. T1Et4iPrIP and $[Fe(T1Et4iPrIP)(OTf)_2]$ (1)

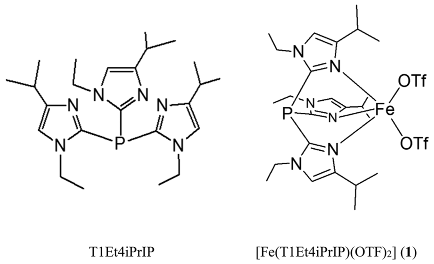

■ RESULTS AND DISCUSSION

Synthesis and Structure. The synthesis of $[Fe^{II}(T1Et4iPrIP)(2\text{-}OH\text{-}AP)(OTf)](OTf)$ (**2**), a ferrous DAD-substrate analogue, was achieved by reacting $[Fe^{II}(T1Et4iPrIP)(OTf)_2]$[19,20] with 1.1 equiv of 2-hydroxyacetophenone (2-OH-AP) in CH_2Cl_2 under a dry nitrogen atmosphere. Layering of ether and placement at −30 °C afforded orange crystals in good yield. $[Fe^{II}(T1Et4iPrIP)(2\text{-}O\text{-}AP)]OTf$ (**3**) was prepared by reacting **1** in CH_2Cl_2 with 1.1 equiv of the potassium salt of 2-hydroxyacetophenone in 1 mL

MeOH. The color of the solution immediately changed to dark cherry red. The solution was filtered, layered with ether, and placed at −30 °C. Cherry red colored crystals were deposited in good yield. The ferric complex, [Fe^{III}(T1Et4iPrIP)(DMF)$_3$](OTf)$_3$, (**4**) was prepared by reacting an iron(III) reagent that we reported ([Fe^{III}(DMF)$_6$](OTf)$_3$)[21] with T1Et4iPrIP in CH_2Cl_2. After ether layering and cooling at −30 °C for 24 h, orange plates were deposited. The X-ray structures for complexes **2**−**4** were determined, and selected collection data is shown in Table S1, while selected metric parameters are shown in Table S2.

Complex **2** was solved in $P2_12_12_1$. The structure could be solved and refined in the centrosymmetric space group *Pbca*; however, *R*1 (strong data) increased from 0.044 to 0.109, and there were multitudes of systematic absence violations with respect to the glide planes. Additionally, the Flack parameter refined to 0.40(1), which also points to the lower symmetry model. Although the centrosymmetric model looks good after disorder refinement and application of SQUEEZE,[22] the better model is in the chiral space group.

The structure of **2** (**2a** and **2b**) shown in Figure 1 reveals iron(II) coordinated in a distorted octahedral geometry with N5 (N11) and O3 (O8) occupying the axial positions, while N1 (N7), N3 (N9), O1 (O6), and O2 (O7) are situated in the equatorial positions. The Fe1−O1$_{carbonyl}$ (Fe2−O6$_{carbonyl}$) bond distance is 2.170(4) Å (2.169(3) Å), while the Fe1−O2$_{alcohol}$ and Fe2−O7$_{alcohol}$ bond distances are only slightly shorter, 2.153(4) and 2.140(3) Å, respectively. The average Fe−N bond distance is 2.175 Å. The values are quite comparable to those previously reported for similar complexes.[19,20] The H atom positioned on O2 and O7 is hydrogen-bonded (O2−H2···O13, 2.631(4) Å; O7−H7···O16, 2.671(5) Å) to the uncoordinated triflate oxygen (see Supporting Information, Table S11).

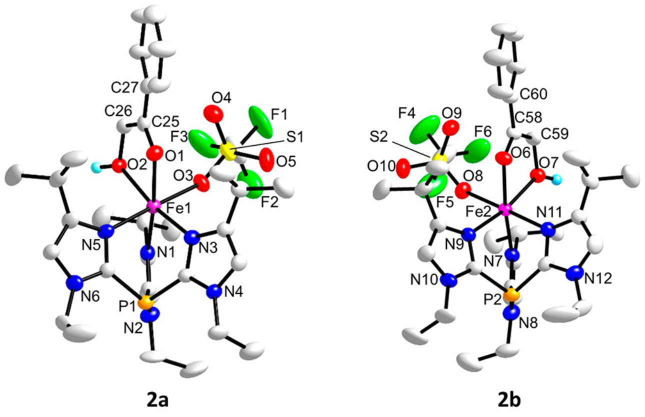

Figure 1. Structures of [Fe^{II}(T1Et4iPrIP)(2-OH-AP)(OTf)]$^+$ (Cation of **2a** and **2b**). H atoms on carbons have been omitted for clarity.

The structure of **3** is shown in Figure 2 and indicates distorted trigonal bipyramidal geometry (*τ* = 0.56)[23] with O1 and N1 serving as axial ligands and N3, N5, and O2 serving as equatorial ligands. The iron-alkoxide ligand (Fe1−O2, 1.913(2) Å) in **3** is clearly shorter than the corresponding iron-alcohol bond (Fe1−O2, 2.153(4) Å) seen in **2**. Interestingly, the Fe1−O1 bond distance in **3** (2.232(2) Å) is elongated by 0.062 Å relative to **2** (2.170(4) Å).

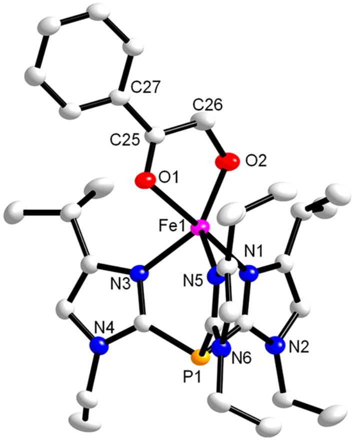

Figure 2. Structures of [Fe^{II}(T1Et4iPrIP)(2-O-AP)]$^+$ (Cation of **3**). H atoms have been omitted for clarity.

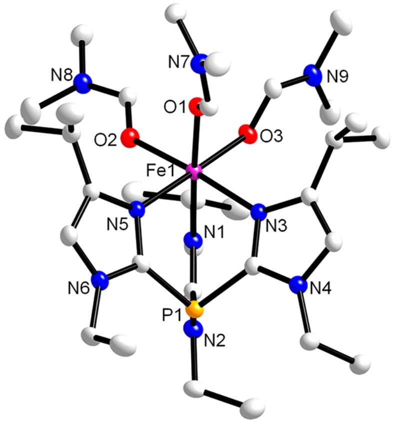

Figure 3. Structures of [Fe^{III}(T1Et4iPrIP)(DMF)$_3$]$^{3+}$ (cation of **4**). H atoms have been omitted for clarity.

Complex **4** contains iron(III) coordinated to tridentate T1Et4iPrIP and three DMF oxygens (Figure 3). In general, the bond distances are quite similar to those in the iron(II) complexes reflecting a geometry that is closer to octahedral. The softer nature of the imidazolyl ligands overall is presumably responsible for the bond distances (Fe−N$_{Avg}$ = 2.140 Å) which are comparable to other hexacoordinate iron(III) complexes bonded to imidazole nitrogens.[24−28]

UV−vis Spectroscopy. An overlay of the UV−vis spectra for complexes **1**−**3** is shown in Figure 4. There are clear differences in absorptions and absorption maxima for these species. The spectrum for **1** exhibits a shoulder at 350 nm (180 M^{-1} cm^{-1}) with no features at 400 nm. Complex **2**, on the other hand, possesses a band at 424 nm (343 M^{-1} cm^{-1}).

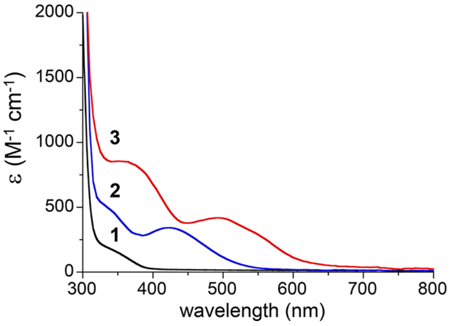

Figure 4. UV−vis spectra for complexes **1**−**3** in CH_2Cl_2 at 25 °C.

When we examine the spectrum of **3**, we observe two bands (361 nm, 855 M^{-1} cm^{-1} and 495 nm, 322 M^{-1} cm^{-1}). The ferric species (**4**, Figure S1) contains bands at 355 (5550 M^{-1} cm^{-1}) and 519 (242 M^{-1} cm^{-1}). These features are very similar to those reported by Enya and co-workers for the ferric form of DAD.[1] It should also be noted that the spectrum reported for the ferric DAD-substrate adduct[1] resembles **2** suggesting that this may actually be the ferrous DAD-substrate adduct (see Reactivity Studies below).

We have recorded the ^{1}H NMR spectrum of **1**, **2**, and the titration of **2** with Et_3N to generate **3** in situ (Figure 5). Peaks related to 2-OH-AP are clearly visible when comparing **1** with **2**. Analysis of paramagnetically shifted peaks indicates that protons (~65 ppm) related to **1** possibly coalesce to a single peak when **2** is formed. A peak at −50 ppm is also observed to become diminished. A smooth conversion between **2** and **3** is observed when Et_3N is added to **2**.

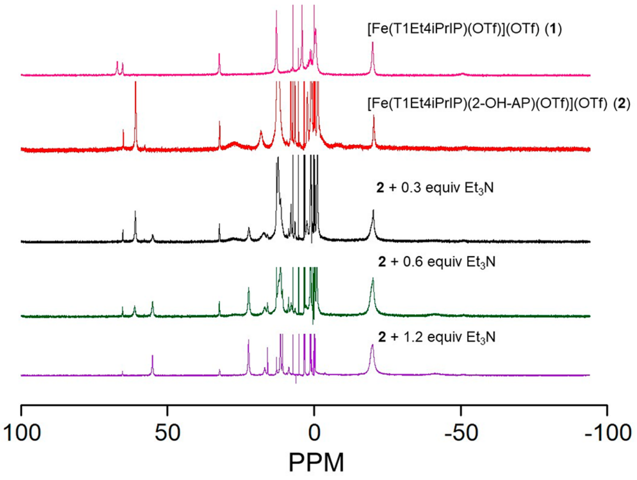

Figure 5. ^{1}H NMR of Complex **1** and Complex **2** titrated with Et_3N in $CDCl_3$ at 25 °C.

Reactivity Studies. Exposure of complexes **2** and **3** to oxygen in CH_2Cl_2 results in 2-OH-AP and 2-O-AP^- scission, respectively, and formation of benzoic and formic acid. The benzoic acid is cleanly observed by NMR, but the formic acid (although observed in the GCMS analysis) is lost during the workup. When $^{18}O_2$ is used, we observe 100% incorporation of O-18 into the products. Analysis of the fragmentation species indicates that the O-18 is present in both the carbonyl and the −OH oxygens (see Figure S2). This is likely due to tautomerization during the workup.[29] The reactions were followed by UV−vis spectroscopy (Figure 6). No intermediates were observed during this process even at low temperature (−80 °C). A plot of ε_{370} vs time for **2** and **3** is shown in Figure 6a. From these profiles, it is clear that **3** reacts with O_2 at a much faster rate compared to **2** and is complete in 3.5 min. Complex **2**, on the other hand, reacts more gradually and is complete after 40 min. The spectrum for oxygenation of **2** (Figure 6b) reveals a gradual increase in absorption between 310 and 500 nm, while for **3** (Figure 6c,d), there is an initial increase in absorption at ~350 and 650 nm followed by a decrease in absorption at ~560 nm exhibiting an isosbestic point at ~410 nm. The reported UV−vis spectrum for the DAD-substrate adduct[1] indicates that a band at ~400 nm decreases during oxygenation, which is the opposite of what we observe. Unlike enzymes, ferrous model complexes have the potential to form μ-oxo or μ-hydroxo species upon oxygenation. The charge transfer bands of these species[30] could obscure the observed decrease of a low molar extinction coefficient band at 400 nm.

When 2-OH-AP substrate is added to **1** in excess (100 equiv) in CH_2Cl_2 at 25 °C and O_2 is bubbled into the mixture, we observed catalytic behavior with multiple turnovers (TON = 13). The EPR spectrum (77 K) of **1** + 2 equiv 2-OH-AP in CH_2Cl_2 after being oxygenated for 14 h exhibited an axial signal at $g \sim 4.3$ and $g \sim 2$. This is consistent with high spin Fe^{3+} but only accounts for a very minor component. Since the absorption spectrum for the catalytic mixture after oxygenation clearly indicates that iron(III) is the final product (Figure 6b), it is likely that the product mixture contains antiferromagnetically coupled iron(III) centers. Complexes **2** and **3** provided similar catalytic behavior with **2** being slightly more active (**2**, TON = 13; **3**, TON = 11). Complex **4**, on the other hand, did not exhibit catalytic behavior under the same conditions suggesting that the active form of DAD is not the ferric state. Since Enya and co-workers reported the anaerobic absorption spectrum of the iron(III)-substrate adduct,[1] we sought to react **4** with 2-OH-AP to isolate the synthetic analogue. We were ultimately unsuccessful in our efforts since it became apparent that the adduct was not stable under anaerobic conditions. The mixture of **4** and 2-OH-AP was monitored by UV−vis spectroscopy and the results are illustrated in Figure 7. Initially, an absorption band for **4** is observed at 355 nm (5550 M^{-1} cm^{-1}). When 2-OH-AP is added, there is a rapid decrease in the intensity of this band with the formation of three isosbestic points at 332, 422, and 505 nm (Figure 7a). The change is presumed to arise from coordination of 2-OH-AP to **4**. The absorption spectrum recorded initially at 1 min intervals, and then 10 min intervals was additionally monitored. As can be seen, there is a continued decrease in the shoulder at 365 nm (Figure 7b). At 155 min (426 nm 371 M^{-1} cm^{-1}), the spectrum begins to resemble that of **2** (Figure 4). This result strongly suggests that the ferric form of DAD is susceptible to anaerobic reduction in the presence of substrate. To further investigate this point, we conducted X-band EPR experiments on **4** in the absence and presence of 2-OH-AP. The results shown in Figure 8a indicate that **4** is Fe(III) high spin ($g \sim 4.3$, $S = 5/2$) with no signal in the $g \sim 2$ region. The mixture of **4** and 2-OH-AP after 155 min, however, is silent, suggesting the formation of iron(II) which supports the formation of **2**; however, one can also imagine an EPR-silent antiferromagnetically coupled diferric species as well. To rule this out, we measured the ^{1}H NMR spectrum of the resulting species (Figure 8b) and found the spectrum to be quite similar to **2** (Figure 5b).

The sluggish nature of this reaction indicates that this process is most likely not critical for catalytic behavior but suggests a mechanism for reducing the ferric form of DAD to the ferrous form, which could then become catalytically active (see below). To test this hypothesis, we reacted **4** with 2 equiv 2-OH-AP in CH_2Cl_2 under nitrogen. After 2.5 h, the mixture was exposed to oxygen for 14 h. Analysis of the reaction mixture indicated that a small amount of benzoic acid (20% based on **4**) was generated. When this reaction was performed under catalytic conditions (100 equiv 2-OH-AP), 8.5 turnovers were observed supporting the suggested mechanism for DAD activation.

Computational Studies. To gain insight into the electronic structures of complexes **2**−**4**, we conducted

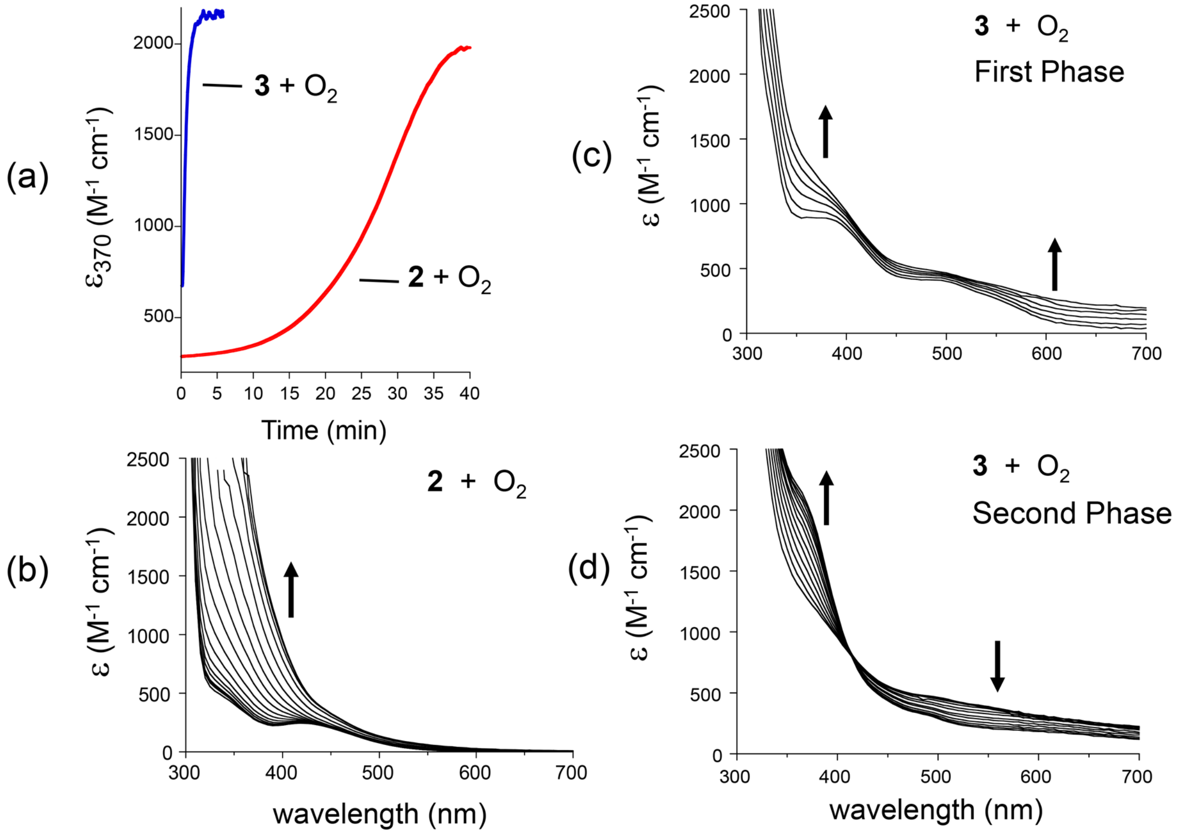

Figure 6. (a) Kinetic trace for the oxygenation of **2** and **3** and changes in the UV−vis spectra for (b) **2** and (c and d) **3** at 22 °C in CH_2Cl_2. Arrows indicate trend in spectral intensity.

theoretical studies using DFT. The geometries of the ground states were optimized, and orbital energies were calculated using B3LYP/6-31G*. The empirical metric parameters for these compounds were compared to calculated values, and the results are shown in Table S2. For **2a**, the greatest deviation for the Fe-ligand bond distance is 0.168 Å; however, this bond distance is associated with the triflate oxygen and is calculated to be shorter than the experimental value, whereas all other calculated values are slightly longer. The greatest difference in Fe−N values is 0.069 Å (Fe2−N7) which is the bond *trans* to the carbonyl ligand. For complexes **3** and **4**, agreement between theoretical and empirical iron−ligand bond distances is quite good with the largest difference being 0.044 Å. Calculated and empirical bond angles are also in close agreement, which gives confidence that the theoretical data is a good representation of the electronic structure for complexes **2**−**4**. In light of these results, we are able to draw conclusions regarding calculated molecular orbital contributions and their energies. Figures S3 and S4 illustrate the HOMO, HOMO−1, LUMO, and LUMO+1 for cations **2** and **3**, respectively. Figure S5 exhibits the HOMO and LUMO orbitals for cations of **4**.

For **2** (Figure S3), it is observed that the highest occupied molecular orbital (HOMO, β-203) is largely distributed over the Fe d_{xy} orbital. HOMO−1 (β-202, α-207) comprises π electrons associated with the imidazole ring of T1Et4iPrIP. The lowest unoccupied molecular orbital (LUMO, β-204) is primarily distributed over p orbitals of the 2-OH-AP ligand. The metal d_{xz}/d_{yz} orbital are associated with LUMO+1 (β-205) along with p orbitals from T1Et4iPrIP. For complex **3** (Figure S4), the HOMO (β-166) is a d_{xy} orbital. The HOMO−1 (α-169), on the other hand, is an antibonding orbital primarily between d_{z2} and alkoxide oxygen p orbitals. The LUMO orbital (α-171) is associated with the 2-O-AP$^-$ ring p orbitals, while the LUMO+1 (β-168) is mainly associated with p orbitals of T1Et4iPrIP.

For complex **4**, the HOMO (α-194) and LUMO (β-190) are provided (Figure S5). The HOMO is constructed from imidazole π orbitals located on T1Et4iPrIP. The LUMO is associated with the Fe d_{xy} orbital.

The HOMO−LUMO gap for **2** (2.99 eV) is the largest in the set, while five-coordinate **3** has a value of 2.51 eV. Complex **4** notably has the smallest value (1.877 eV) which is consistent with the presence of a hard iron(III) cation bonding with soft imidazole nitrogen and carbonyl oxygen ligands.

Electronic Absorption Calculations. The TD-DFT calculated absorption spectra of **2** and **3** matched reasonably with the experimental absorption spectrum. The calculated spectrum of **3** (Figure 9) shows features at 570 and 403 nm, which are in good agreement with the experimental absorption maxima of **3** at 495 and 361 nm (Figure 4). The TD-DFT calculated absorption spectrum of **3** also predicts an additional feature at 320 nm. The calculated absorption spectrum of **2** (Figure 10) shows a band at 515 nm. While the frequency of this band is in reasonable agreement with the experimental spectrum, the calculated intensity is remarkably low (ε = 30 M^{-1} cm^{-1}). Because of this less-than-optimal agreement between experiment and theory, we also calculated the absorption spectrum for a five-coordinate model of **2** lacking the triflate ligand. We refer to this model as **2′**, and the TD-DFT computed absorption spectrum of this model is shown in Figure 11. In this case, the calculated spectrum shows relatively

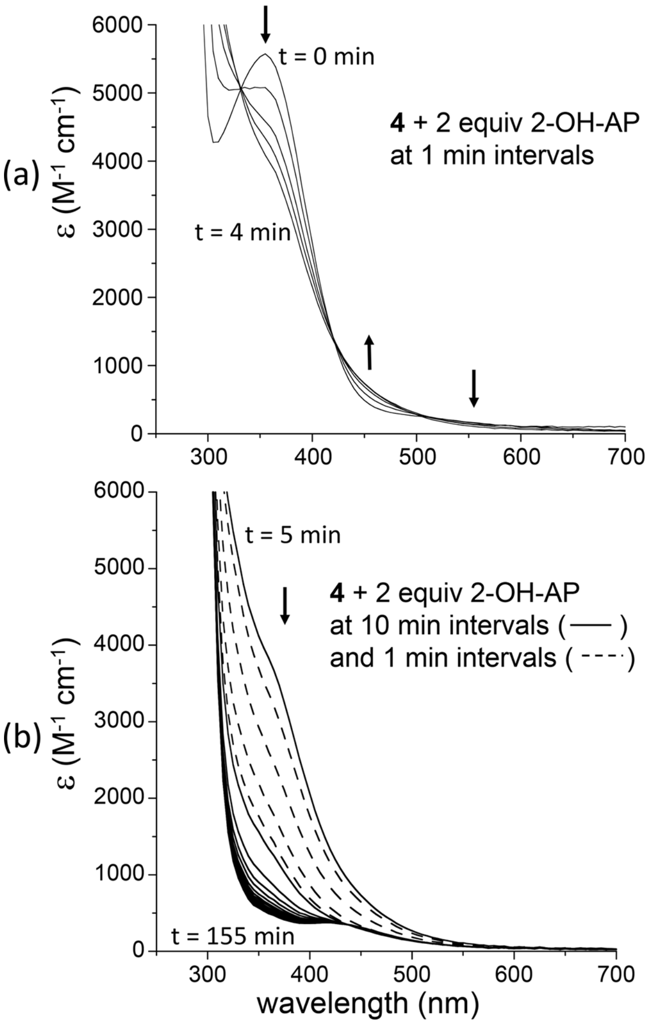

Figure 7. Changes in the optical spectrum for the addition of 2 equiv 2-OH-AP to **4** in CH_2Cl_2 at 25 °C (a) between 0 and 4 min (at 1 min intervals) and (b) between 5 and 155 min (at intervals indicated).

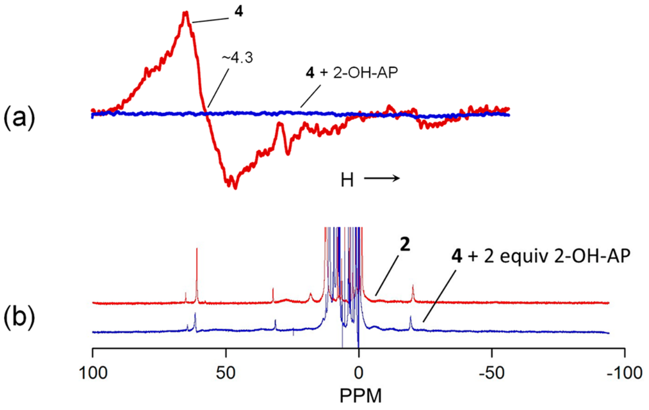

Figure 8. (a) X-band EPR spectrum of **4** (red —) and **4** + 2 equiv 2-OH-AP (blue —) in frozen CH_2Cl_2 (77 K) and (b) ^1H NMR spectrum of the final species after 2 equiv 2-OH-AP is added to **4** (blue —) compared to **2** in $CDCl_3$ at 25 °C. EPR: Selected *g* values are indicated. Spectrometer settings: microwave frequency 9.3 GHz; microwave power, 0.22 mW; modulation frequency, 100 kHz; modulation amplitude, 8 G; gain, 2.5×10^4. [**4**] = 5 mM.

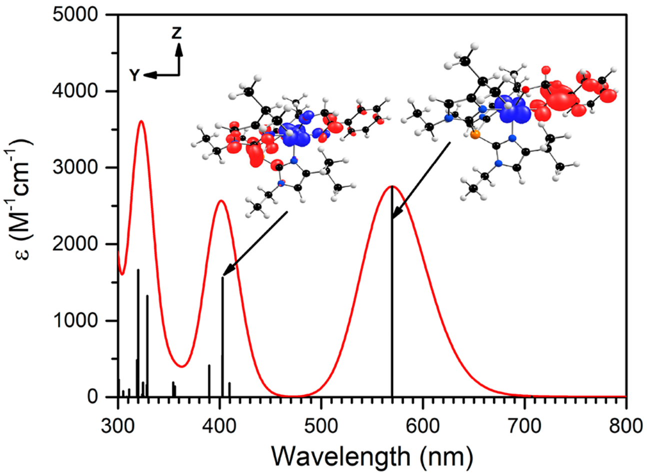

Figure 9. TD-DFT computed absorption spectrum for **3**. The sticks indicate the electronic transitions, with the corresponding electron-density difference maps (EDDMs) for two prominent transitions shown in the inset. Red and blue colors in the EDDMs denote gain and loss of electron density, respectively.

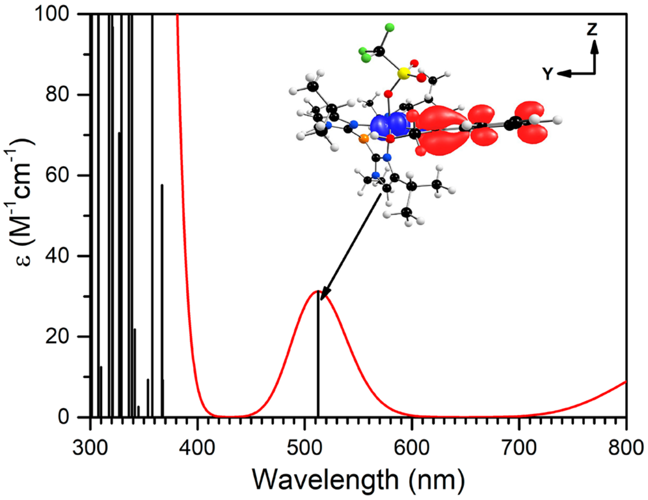

Figure 10. TD-DFT computed absorption spectrum for **2**. The sticks indicate the allowed electronic transitions with their corresponding EDDMs. Red and blue colors in the EDDMs denotes gain and loss of electron density, respectively.

intense bands at 515 and 336 nm, with a shoulder near 390 nm, while the experimental absorption spectrum of **2** shows a band at 424 nm and a poorly resolved band in the range of 320−370 nm (Figure 4). Therefore, we obtain better agreement with experiment for five-coordinate **2′** than for six-coordinate **2**.

The 570 nm band in the TD-DFT calculated spectrum of **3** is a metal-to-ligand charge transfer (MLCT) band that arises from a one-electron excitation from the Fe^{II} $3d_{xy}$ HOMO to the π-type LUMO centered on the 2-O-AP ligand (Figure 9 and Tables S3 and S4). The band at 403 nm also arises from a MLCT transition (Figure 9, Tables S3 and S4). This electronic transition involves the same Fe^{II} $3d_{xy}$ HOMO as the transition at 570 nm, but the acceptor MO is primarily localized on the T1Et4iPrIP ligand (LUMO+1), with some admixture from π-type orbitals on the 2-O-AP ligand. The TD-DFT calculations for this transition also reveal some minor admixture of intraligand charge transfer (ILCT) and ligand-to-ligand charge transfer (LLCT), as summarized in Tables S3 and S4. The optical absorption features of **3** are therefore dominated by the

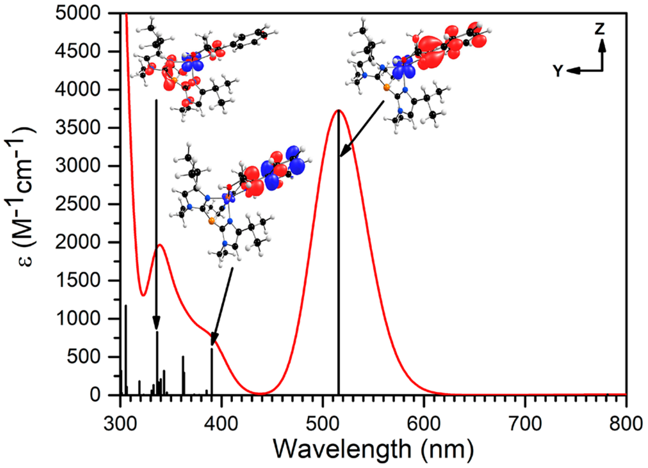

Figure 11. TD-DFT computed absorption spectrum for **2′**, which is a five-coordinate variant of **2** lacking the triflate ligand. The sticks indicate the allowed electronic transitions with their corresponding EDDMs. Red and blue colors in the EDDMs denotes gain and loss of electron density, respectively.

frontier MOs, which are π-type orbitals on the metal and ligands.

In the TD-DFT calculated spectrum of **2** (Figure 10), the band at 515 nm is an MLCT band arising from a one-electron transition from a molecular orbital with mainly Fe^{II} 3d_{xy} character to a π-type MO of the 2-OH-AP ligand. However, the presence of the triflate ligand leads to a tilting of the relevant Fe^{II}- and 2-OH-AP-based HOMO and LUMO, respectively, such that these MOs no longer have optimal overlap. This attenuated overlap leads to the predicted low intensity of this transition (Figure 10). In contrast, removal of the triflate ion in **2′** provides metal−ligand interactions similar to those of **3**, and the intense, lowest-energy absorption band arises from a MLCT from the Fe^{II} 3d_{xz} MO to the π-type acceptor MO of the 2-OH-AP ligand (Figure 11). The band at 336 nm is also an MLCT band involving a one-electron excitation from an Fe^{II} 3d_{xz} MO to π-type MOs mainly of the T1Et4iPrIP ligand and some of the 2-OH-AP ligand. This excitation also contains some Fe^{II} d−d character. The shoulder at 390 nm arise from a one-electron excitation essentially resulting from an ILCT within the 2-OH-AP ligand system, mixed with some MLCT (Fe^{II} 3d_{xz} MO to a π-type MO of the 2-OH-AP ligand) and LLCT (Figure 11 and Tables S3 and S4).

The TD-DFT computations are also able to provide insight into the basis for the red-shift of the MLCT transition for **3**. The protonated 2-OH-AP ligand in **2′** (and **2**) has two prominent consequences. First, the π-based 2-OH-AP MO of **2′** (and **2**) is at lower energy than the corresponding MO of 2-O-AP in **3** (Figure 12). Second, the greater charge donation from the anionic 2-O-AP ligand to the Fe^{II} center in **3** reduces the Lewis acidity of the Fe^{II} center, which causes Fe^{II} 3d manifold of **3** to be destabilized relative to that of **2′** (and **2**). As shown in Figure 12, the shift in the Fe^{II} 3d manifold is the dominant perturbation, accounting for the red-shift in the MLCT band for **3**. These computations demonstrate that protonation of the 2-O-AP ligand has a dramatic effect on the Lewis acidity of the Fe^{II} center, which could be employed by the enzyme as a mechanism to tune the reactivity of the active-site metal center.

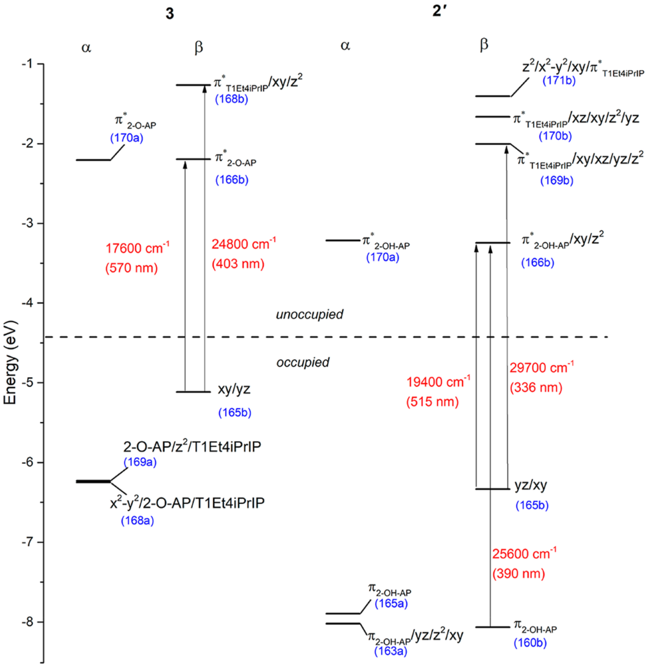

Figure 12. MO energy diagram for **2′** (right) and **3** (left).

Proposed Mechanism for Catalytic Oxidation of 2-OH-AP by Complex 1. It has been proposed by Enya and co-workers that the catalytically competent form of DAD is the iron(III) form of the enzyme.[1] It is indicated that iron(III) binds to 2-OH-AP in the deprotonated form to generate a radical and iron(II) (Scheme 2). This species is then believed to react with oxygen to generate an iron(III)-alkylperoxo species. Decomposition of this species yields oxygenated products. In our hands, the iron(II) complex (**1**) is catalytically competent and not iron(III) (**4**).

Most investigators have invoked the initial reaction of iron(II) (coordinated by deprotonated substrate) with oxygen to generate a superoxo intermediate.[7,10,15,16] H atom abstraction by the superoxo group from the α C−H group of the substrate[31,32] is said to result in formation of a ferric hydroperoxo species (Fe^{III}−OOH) which then becomes transferred to the ligand via a rebound mechanism. Based on the isolation and characterization of **2** and its UV−vis resemblance to the DAD iron(II)-substrate complex, we propose a slightly modified mechanism. Although we find no evidence for the formation of either a superoxo or hydroperoxo intermediate (Figure 6), such species could be sufficiently short-lived as to not be observable under reaction conditions. In our mechanism (Scheme 4), the iron(II) mimic for DAD (**1**) binds the substrate and reacts with oxygen to generate an iron(III)-superoxo species which subsequently abstracts an H atom from the substrate to yield a Fe^{III}−OOH species and a carbon radical. Transfer of the hydroperoxyl (Scheme 4, **I**) species to the carbon radical was suggested by Paine and co-workers.[15] Rearrangement of this species yields a dioxetane (Scheme 4, **II**) which then collapses to the scission product (Scheme 4, **III**).[18,33−36] The GCMS data (Figure S2) indicates that the O-18 in the products tautomerize to give O-18 at both the carbonyl and hydroxyl oxygens which is likely to occur during workup.[29] In this proposed mechanism, benzoic acid and formic acid are generated in their *protonated* forms thus negating the need for initial deprotonation of the substrate.

Scheme 4. Proposed Catalytic Mechanism for Oxidation of 2-OH-AP by 1[15]

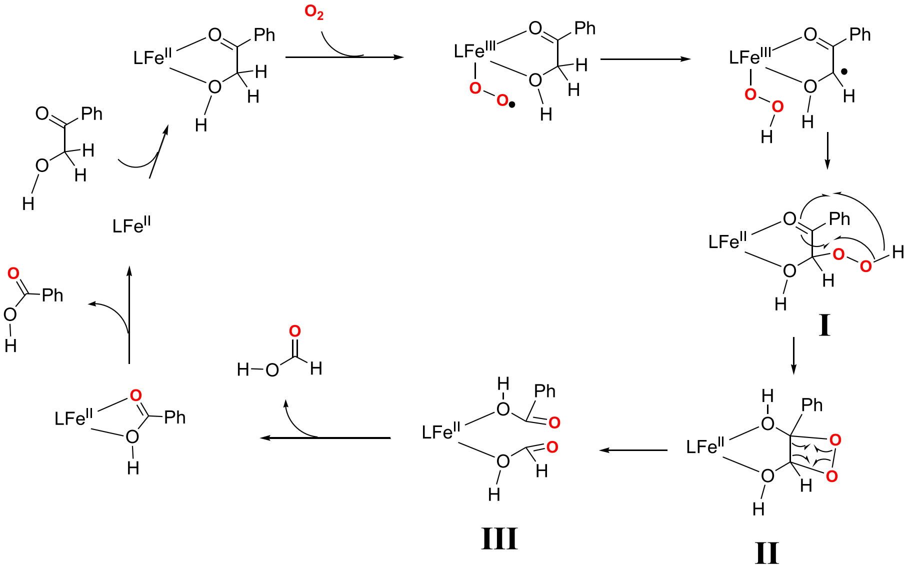

After release of the products, the iron(II) complex is primed for additional turnovers.

■ CONCLUSIONS

In our efforts to clarify the operative mechanism for the mononuclear nonheme enzyme DAD, we synthesized and structurally characterized three iron complexes supported by a neutral trisimidazolyl phosphine ligand designed to more accurately mimic a trishistidinyl protein metal binding site compared to negatively charged trispyrazolylborate ligands. Such a ligand system provides model complexes that closely mimic the spectroscopy and catalytic activity of DAD. By utilizing the substrate analogues 2-hydroxyacetophenone (2-OH-AP) and deprotonated 2-hydroxyacetophenone (2-O-AP$^-$), we were able to synthesize the metal complex−substrate adducts and compare the structural and spectroscopic properties to those of the enzyme. We have also synthesized [Fe^{III}(T1Et4iPrIP)(DMF)$_3$](OTf)$_3$ (**4**) and found that it does not react with 2-OH-AP to generate products catalytically like the Fe(II) species. However, when **4** is anaerobically incubated with 2 equiv 2-OH-AP, it is reduced to **2**, which is now catalytically competent. These results have led us to suggest a mechanism for the catalytic oxidation of that involves initial binding of the substrate in the *protonated* form followed by oxygen-induced scission of the substrate to yield products and the activated Fe(II) species. DFT studies also reveal that complex **2** is the most thermodynamically stable complex in the set in the absence of oxygen. TD-DFT calculations suggest that **2** loses its OTf$^-$ ligand in solution providing a 5-coordinate species (**2′**). The calculations also reveal that low energy absorptions for **2** (**2′**) and **3** arise from MLCT transitions.

■ EXPERIMENTAL SECTION

Materials and Methods. 2-Hydroxyacetophenone (2-OH-AP) was purchased from Sigma-Aldrich Chemical Co. *N*,*O*-Bistrifluoroacetamide (BSTFA) was purchased from Supelco. Fe(OTf)$_2$·2CH$_3$CN was obtained according to a literature procrdure.[37] [Fe(T1Et4iPrIP)(OTf)$_2$] was prepared according to a published method.[19] The potassium salt of 2-hydroxyacetophenone was prepared by reacting 1.1 equiv KOH with 2-OH-AP in methanol under nitrogen and then removing the solvent in vacuo. Oxygen (99.6%) was procured from Praxair, and Oxygen-18 was purchased from ICON-Isotopes, 98.2 atom %. CDCl$_3$ was obtained from Cambridge Isotopes Laboratories, Inc. All other reagents were purchased from commercial sources and used as received. Pure dry solvents were acquired using an Innovative Technologies, Inc. Solvent Purification System. Air-sensitive manipulations were performed using an Innovative Technologies, Inc. nitrogen-filled glovebox or standard Schlenk-line techniques. Elemental analysis was performed on pulverized crystalline samples that were placed under vacuum and sealed in glass ampules prior to submission (Atlantic Microlabs, Inc., Norcross, GA).

Synthesis. *[Fe(T1Et4iPrIP)(2-OH-AP)(OTf)](OTf) (**2**).* To a stirring solution of [Fe(T1Et4iPrIP)(OTf)$_2$] (82 mg, 0.103 mmol) in 2 mL CH$_2$Cl$_2$ was added 2-hydroxyacetophenone (15.4 mg, 0.113 mmol) dissolved in 1 mL CH$_2$Cl$_2$. After 1 h of stirring, the reddish orange solution was filtered and layered with diethyl ether. The solution was then placed at −30 °C. After 24 h, reddish orange crystals were deposited. The crystals were collected and washed with ether. Yield: 60 mg (62.4%). Anal. Calcd for $C_{34}H_{47}F_6FeN_6O_8PS_2$ (**2**): C, 43.78; H, 5.08; N, 9.01. Found: C, 43.27; H, 5.16; N, 8.92. FTIR (cm^{-1}, intense bands only): 3141 (w), 2972 (w), 2874 (w), 1658 (s, νC=O$_{asym}$), 1598 (s), 1555 (m), 1451 (m, νC=O$_{sym}$), 1385 (m), 1289 (m, νSO$_{3asym(bonded)}$), 1219 (m, νCF$_{3sym}$), 1155 (s, νCF$_{3asym}$), 1087 (w), 1026 (s, νSO$_{3sym}$), 810 (w), 759 (s), 728 (s), 671 (w), 634 (s), 570 (m), 538 (w), 516 (s) cm^{-1}. UV−vis (CH$_2$Cl$_2$) [λ_{max}, nm (ε, M^{-1} cm^{-1})]: 340 (473, sh), 424 (343).

*[Fe(T1Et4iPrIP)(2-O-AP)](OTf) (**3**).* To a stirring solution of [Fe(T1Et4iPrIP)(OTf)$_2$] (50 mg, 0.063 mmol) in 2 mL CH$_2$Cl$_2$ was added the potassium salt of 2-hydroxyacetophenone (12.1 mg, 0.069 mmol) in 1 mL MeOH. The color of the solution immediately changed to a dark cherry red. After 1 h of stirring, the solution was filtered, and the solvent was removed under vacuum. The residue was redissolved in 2 mL CH$_2$Cl$_2$ and layered with diethyl ether. The solution was then placed at −30 °C. After 72 h, cherry red colored crystals were deposited. The crystals were collected and washed with ether. Yield: 30 mg (61%) Anal. Calcd for $C_{33}H_{46}F_3FeN_6O_5PS$ (**3**): C, 50.64; H, 5.92; N, 10.47. Found: C, 50.69; H, 5.92; N, 10.50. FTIR (cm^{-1}, intense bands only): 3135 (w), 2964 (w), 2873 (w), 1640 (s, νC=O$_{asym}$), 1553 (s), 1473 (m, νC=O$_{sym}$), 1385 (m), 1259 (m, νSO$_{3asym(nonbonded)}$), 1222 (s, νCF$_{3sym}$), 1140 (w, νCF$_{3asym}$), 1084 (w), 1029 (s, νSO$_{3sym}$), 987 (m), 799 (m), 754 (s), 726 (s), 689 (s), 673 (w), 636 (s), 571 (s), 537 (w), 516 (s) 492 (m) cm^{-1}. UV−vis (CH$_2$Cl$_2$) [λ_{max}, nm (ε, M^{-1} cm^{-1})]: 361 (855), 495 (322).

[Fe(T1Et4iPrIP)(DMF)$_3$](OTf)$_3$ (4). To a stirring solution of Fe(DMF)$_6$(OTf)$_3$ (115 mg, 0.116 mmol) in 2 mL CH_2Cl_2 was added T1Et4iPrIP (54 mg, 0.122 mmol) dissolved in 2 mL CH_2Cl_2. The color of the solution was yellowish brown. After 1 h of stirring, the solution was filtered and layered with diethyl ether. The solution was then placed at −30 °C. After 1 d, light brown crystals were deposited. The crystals were collected and washed with ether. Yield: 105 mg (77%). FTIR (cm^{-1}, intense bands only): 3137 (w), 3091 (w), 2966 (w), 1713 (s), 1640 (m, νC=O$_{asym}$), 1524 (s), 1435 (m, νC=O$_{sym}$), 1356 (s), 1260 (m, $\nu SO_{3asym(nonbonded)}$), 1140 (s, νCF_{3asym}), 1025 (s, νSO_{3sym}), 971 (w), 698 (w), 631 (s), 571 (s), 541 (m), 514 (s) 479 (m), 403 (m) cm^{-1}. UV−vis (CH_2Cl_2) [λ_{max}, nm (ε, M^{-1} cm^{-1})]: 272 (30,000), 355 (5550), 519 (242). Anal. Calcd for [Fe(T1Et4iPrIP)(DMF)$_2$](OTf)$_3$, $C_{33}H_{53}F_9FeN_8O_{11}PS_3$ (Elemental analysis indicates that one DMF is removed from **4** when the sample is heated at 40 °C under high vacuum): C, 36.30; H, 4.89; N, 10.26. Found: C, 36.40; H, 4.94; N, 10.50.

Physical Characterization. ^{1}H NMR spectra were recorded at 25 °C on a Bruker Avance II 400 MHz instrument and sample peaks in [D]dichloromethane were referenced to TMS (tetramethylsilane). FT-IR spectra were measured on a Bruker ATR Alpha P spectrometer. Optical spectra were collected on a Cary 50 UV−vis spectrophotometer. GCMS experiments were performed on an HP 6890/5973 GCMS. EPR spectra were recorded on a Varian Century series X-band (9.3 GHz) spectrometer with a E-4531 dual-cavity, 9 in. magnet, and a 200 mW Klystron. Special recording was carried out by employing ESRTAK software that was developed at OU. All EPR spectra were recorded at 77 K. A 1 mM Fe^{III}/EDTA solution [prepared by stirring $FeCl_3 \cdot 6H_2O$ with excess $Na_2EDTA \cdot 2H_2O$ (Aldrich) for several hours] was used to calculate the spins and g values in the $g \approx 4.3$ region.

Reactivity Studies. The stoichiometric reactions were carried out in a fume hood at 22 °C. To a 25 mL Schlenk flask was added 0.04 mmol of **2** or **3** dissolved in 4 mL CH_2Cl_2 under nitrogen. The flask was stoppered then sparged with oxygen (Airgas, Industrial grade) or oxygen-18 (ICON Isotopes, 98.2 atom %) for 2 min. After stoppering, the solution was stirred for 14 h. 4 mL of 2 M HCl was then added and the mixture was shaken. The organic layer was separated, and the aqueous layer was further extracted (3× with 3 mL CH_2Cl_2). The organic layers were combined and dried over sodium sulfate. The solvent was then evaporated in vacuo. The resulting solid was redissolved in 1 mL CH_2Cl_2 and naphthalene (internal standard) and 10 equiv BSTFA (*N,O*-Bis(trimethylsilyl)trifluoro-acetamide, Supelco) were added. Solutions were then analyzed by GCMS. Trimethylsilylbenzoate was quantified using an authentic standard (containing naphthalene as the internal standard). The catalytic reactions (containing 100 equiv 2-OH-AP) were quantified in a similar manner. Control reactions using $Fe(ClO_4)_2 \cdot 6H_2O$ and $Fe(OTf)_2 \cdot 2CH_3CN$ were used in place of the catalysts and yielded ∼1 equiv of benzoic acid product under the catalytic conditions described above.

Computational Details. To characterize the electronic structure of **2**−**4**, we performed DFT studies using the GAUSSIAN09 (Rev. C.01) program package.[38] These calculations provided the energy minimized molecular geometries, molecular orbitals (HOMO−LUMO), and vibrational spectra. We employed the functional B3LYP. The basis set used was 6-31G(d).[39] The initial coordinates were taken from the X-ray data. The default convergence criteria was applied and the geometry was optimized in the quintet state without any constraints. Local minima were confirmed for the optimized structure. A comparison between selected calculated and experimental metric parameters is given in Table S2. The program Avogadro[40] (an open-source molecular builder and visualization tool, ver. 1.1.0. http://avogadro.openmolecules.net/) was used to generate the molecular orbitals. Electronic absorption spectra were calculated using the time-dependent density functional theory (TD-DFT) method, as implemented in the ORCA 4.2.1 computational software package.[41] The TD-DFT calculation was performed using the B3LYP functional[42−44] with the Ahlrichs def2-TZVP basis set for iron, nitrogen, phosphorus, and oxygen atoms; while the def2-SVP basis set[45,46] was used for carbon and hydrogen atoms. The RIJCOSX approximation[47,48] was utilized with the def2/J auxiliary basis sets. Dichloromethane solvation was accounted for using the CPCM continuum solvation model.[49] An integration grid of 5 and final grid of 6, with tight SCF convergence criteria, were employed. The isosurface plots of the electron density difference maps EDDMs were generated in the Chemcraft program[50] using a contour value of 0.003.

X-ray Crystallography. Compounds **2**−**4** were crystallized from a dichloromethane/ether solution. Complex **2** was placed onto the tip of a thin glass optical fiber and mounted on a Bruker SMART APEX II CCD platform diffractometer for a data collection.[51] A preliminary set of cell constants and an orientation matrix were calculated from reflections harvested from three orthogonal wedges of reciprocal space. The full data collection was carried out using Mo Kα radiation (graphite monochromator) with a frame time of 50 s and a detector distance of 3.98 cm. A randomly oriented region of reciprocal space was surveyed: six major sections of frames were collected with 0.50° steps in ω at six different ϕ settings and a detector position of −38° in 2θ. The intensity data were corrected for absorption.[52] Final cell constants were calculated from the *xyz* centroids of strong reflections from the actual data collection after integration.[53] See Table S1 for additional crystal and refinement information. The structure was solved using SHELXT-2014/5[54] and refined using SHELXL-2017/1.[55] The space group $P2_12_12_1$ was determined based on systematic absences and intensity statistics. The structure could be solved and refined in centrosymmetric space group *Pbca*; however, *R*1 (strong data) increased from 0.044 to 0.109, and there were multitudes of systematic absence violations with respect to the glide planes. All hydrogen atoms were placed in ideal positions and refined as riding atoms with relative isotropic displacement parameters. Reflection contributions from highly disordered solvent (an apparent mixture of dichloromethane and diethyl ether) were fixed and added to the calculated structure factors using the SQUEEZE routine of program Platon,[23] which determined there to be 854 electrons in 2972 Å^3 treated this way. Because the exact identity and amount of solvent were unknown, no solvent was included in the atom list or molecular formula. Thus, all calculated quantities derived from the molecular formula (e.g., F(000), density, molecular weight, etc.) are known to be incorrect. The crystal was an inversion twin whose component mass ratio refined to 0.60:0.40. One ethyl group and the CF_3 groups of two triflate ligands were modeled as disordered over two positions each: C7−C8, 0.75:0.25; C33/F1−F3, 0.67:0.33; C66/F4−F6, 0.73:0.27. The hydroxyl groups of the bidentate ligands are hydrogen bonded to the uncoordinated triflate anions.

Crystals of **3** and **4** were placed onto a thin glass optical fiber or a nylon loop and mounted on a XtaLab Synergy-S Dualflex diffractometer equipped with a HyPix-6000HE HPC area detector for data collection at 99.99(10) K and 100.0(10) K for **3** and **4**, respectively. A preliminary set of cell constants and an orientation matrix were calculated from a small sampling of reflections.[5,6] A short pre-experiment was run, from which an optimal data collection strategy was determined. The full data collection was carried out using a PhotonJet (Cu) X-ray Source and a detector distance of 31.2 mm. Series of frames were collected in 0.50° steps in ω at different 2θ, κ, and ϕ settings. After the intensity data were corrected for absorption, the final cell constants were calculated from the *xyz* centroids of strong reflections from the actual data collection after integration.[56] The structures were solved using ShelXT[55] and refined using ShelXL.[57] The space groups were determined based on intensity statistics. Most or all the non-hydrogen atoms were assigned from the solution. Full-matrix least-squares/difference Fourier cycles were performed, which located any remaining non-hydrogen atoms. All non-hydrogen atoms were refined with anisotropic displacement parameters.

For **3**, the crystal was composed of two components with minimal overlap. However, the refinement improved when the intensity data were scaled and reduced (Rigaku Oxford Diffraction, 2018) according to non-merohedral twin law [0.997 0.022 −0.065 / −0.007 1.007 0.021 / 0.081 0.005 0.991], a 180° rotation around reciprocal lattice [0.022 −0.950 −0.312]. There were 7940 unique separate reflections in the first component, 7912 unique separate reflections in the second component, and 663 unique overlapping reflections. Without twin modeling, *R*1 (strong data) refined to 0.063. The mass ratio of components refined to 0.64:0.36. The occupancy of the solvent molecule refined to 0.45, and the symmetry equivalent molecule generated by the nearby crystallographic inversion center is outside of the van der Waals radii of the atoms. One isopropyl group is modeled as disordered over two positions (0.79:0.21).

For **4**, the asymmetric unit contains one tricationic iron complex, three triflate anions, and two cocrystallized dichloromethane solvent molecules, all in general positions. The solvent molecules are modeled as disordered over three positions (Cl1−C37−Cl2, 0.66:0.18:0.16) and two positions (Cl3−C38−Cl4, 0.91:0.09). See Table S1 for additional crystal and refinement information for complexes **2**−**4**.

■ ASSOCIATED CONTENT

Supporting Information

The Supporting Information is available free of charge at https://pubs.acs.org/doi/10.1021/acs.inorgchem.1c00167.

> Experimental data and crystallographic information for **2**−**4** (PDF)

Accession Codes

CCDC 1831279−1831281 contain the supplementary crystallographic data for this paper. These data can be obtained free of charge via www.ccdc.cam.ac.uk/data_request/cif, or by emailing data_request@ccdc.cam.ac.uk, or by contacting The Cambridge Crystallographic Data Centre, 12 Union Road, Cambridge CB2 1EZ, UK; fax: +44 1223 336033.

■ AUTHOR INFORMATION

Corresponding Author

Ferman A. Chavez − *Department of Chemistry, Oakland University, Rochester, Michigan 48309-4477, United States;* orcid.org/0000-0002-5716-0916; Email: chavez@oakland.edu

Authors

Atanu Banerjee − *Dr. K. C. Patel R & D Centre, Charotar University of Science and Technology (CHARUSAT), 388421 Anand, Gujrat, India*

Jia Li − *Department of Chemistry, Oakland University, Rochester, Michigan 48309-4477, United States*

Monika A. Molenda − *Department of Chemistry, Oakland University, Rochester, Michigan 48309-4477, United States*

Adedamola A. Opalade − *Department of Chemistry and Center for Environmentally Beneficial Catalysis, The University of Kansas, Lawrence, Kansas 66045, United States*

Amitava Adhikary − *Department of Chemistry, Oakland University, Rochester, Michigan 48309-4477, United States;* orcid.org/0000-0001-9024-9579

William W. Brennessel − *Department of Chemistry, University of Rochester, Rochester, New York 14627-0216, United States;* orcid.org/0000-0001-5461-1825

Aramice Y. S. Malkhasian − *Department of Chemistry, King Abdulaziz University, Jeddah 21589, Saudi Arabia*

Timothy A. Jackson − *Department of Chemistry and Center for Environmentally Beneficial Catalysis, The University of Kansas, Lawrence, Kansas 66045, United States;* orcid.org/0000-0002-3529-2715

Complete contact information is available at: https://pubs.acs.org/10.1021/acs.inorgchem.1c00167

Notes

The authors declare no competing financial interest.

■ ACKNOWLEDGMENTS

FAC acknowledges the receipt of an OU-REF grant. JL acknowledges a graduate fellowship from OU. MAM acknowledges an OU Provost Award. We thank Prof. M. M. Szczęśniak for assistance with the DFT calculations. NIH Grant No. R15GM112395 and NSF Grant No. CHE-0748607 and CHE-0821487 are gratefully acknowledged. AA thanks the National Cancer Institute of the National Institutes of Health (Grant R01CA045424) for support. AA is also grateful to Research Excellence Fund (REF) and Center for Biomedical Research (CBR) at Oakland University for support. TAJ acknowledges support from NSF (CHE-1900384).

■ REFERENCES

(1) Enya, M.; Aoyagi, K.; Hishikawa, Y.; Yoshimura, A.; Mitsukura, K.; Maruyama, K. Molecular and Catalytic Properties of 2,4 ’-Dihydroxyacetophenone Dioxygenase from *Burkholderia* sp AZ11. *Biosci., Biotechnol., Biochem.* **2012**, *76*, 567−574.

(2) Spivack, J.; Leib, T. K.; Lobos, J. H. Novel Pathway for Bacterial Metabolism of Bisphenol A. Rearrangements and Stilbene Cleavage in Bisphenol A Metabolism. *J. Biol. Chem.* **1994**, *269*, 7323−7329.

(3) Hopper, D. J.; Jones, H. G.; Elmorsi, E. A.; Rhodesroberts, M. E. The Catabolism of 4-Hydroxyacetophenone by an *Alcaligenes* Sp. *Microbiology* **1985**, *131*, 1807−1814.

(4) Hopper, D. J. Oxygenase properties of the (4-hydroxybenzoyl)-methanol-cleavage enzyme from an *Alcaligenes* sp. *Biochem. J.* **1986**, *239*, 469−472.

(5) Hopper, D. J.; Kaderbhai, M. A. 2,4 ’-Dihydroxyacetophenone dioxygenase (EC 1.13.11.41) from *Alcaligenes* sp 4HAP: a novel enzyme with an atypical dioxygenase sequence. *Biochem. J.* **1999**, *344*, 397−402.

(6) Costas, M.; Mehn, M. P.; Jensen, M. P.; Que, L. Dioxygen Activation at Mononuclear Nonheme Iron Active Sites: Enzymes, Models, and Intermediates. *Chem. Rev.* **2004**, *104*, 939−986.

(7) Allpress, C. J.; Berreau, L. M. Oxidative aliphatic carbon-carbon bond cleavage reactions. *Coord. Chem. Rev.* **2013**, *257*, 3005−3029.

(8) Roberts, K. M.; Connor, G. C.; Cave, C. H.; Rowe, G. T.; Page, C. A. The Metal- and Substrate-Dependences of 2,4'-Dihydroxyacetophenone Dioxygenase. *Arch. Biochem. Biophys.* **2020**, *691*, 108441.

(9) Bhattacharya, S.; Rahaman, R.; Chatterjee, S.; Paine, T. K. Aliphatic C-C Bond Cleavage in alpha-Hydroxy Ketones by a Dioxygen-Derived Nucleophilic Iron-Oxygen Oxidant. *Chem. - Eur. J.* **2017**, *23*, 3815−3818.

(10) Keegan, R.; Lebedev, A.; Erskine, P.; Guo, J.; Wood, S. P.; Hopper, D. J.; Rigby, S. E. J.; Cooper, J. B. Structure of the 2,4′-dihydroxyacetophenone dioxygenase from *Alcaligenes* sp. 4HAP. *Acta Crystallogr., Sect. D: Biol. Crystallogr.* **2014**, *70*, 2444−2454.

(11) Guo, J.; Erskine, P.; Coker, A. R.; Gor, J.; Perkins, S. J.; Wood, S. P.; Cooper, J. B. Extension of resolution and oligomerization-state studies of 2,4′-dihydroxyacetophenone dioxygenase from *Alcaligenes* sp. 4HAP. *Acta Crystallogr., Sect. F: Struct. Biol. Commun.* **2015**, *71*, 1258−1263.

(12) Li, J. Synthetic Model Studies for Iron Dioxygenase Enzymes. Ph.D. Dissertation, Oakland University, Rochester, Michigan, 2015.

(13) Xin, M. T.; Bugg, T. D. H. Evidence from Mechanistic Probes for Distinct Hydroperoxide Rearrangement Mechanisms in the Intradiol and Extradiol Catechol Dioxygenases. *J. Am. Chem. Soc.* **2008**, *130*, 10422−10430.

(14) Zhang, S. J.; Wang, X. Y.; Liu, Y. J. Cleavage mechanism of the aliphatic C-C bond catalyzed by 2,4′-dihydroxyacetophenone dioxygenase from *Alcaligenes* sp. 4HAP: a QM/MM study. *Catal. Sci. Technol.* **2017**, *7*, 911−922.

(15) Paria, S.; Halder, P.; Paine, T. K. Oxidative Carbon-Carbon Bond Cleavage of a α-Hydroxy Ketone by a Functional Model of 2,4′-

Dihydroxyacetophenone Dioxygenase. *Angew. Chem., Int. Ed.* **2012**, *51*, 6195−6199.

(16) Manna, R. N.; Malakar, T.; Jana, B.; Paul, A. Unraveling the Crucial Role of Single Active Water Molecule in the Oxidative Cleavage of Aliphatic C−C Bond of 2,4′-Dihydroxyacetophenone Catalyzed by 2,4′-Dihydroxyacetophenone Dioxygenase Enzyme: A Quantum Mechanics/Molecular Mechanics Investigation. *ACS Catal.* **2018**, *8*, 10043−10050.

(17) Rahaman, R.; Paria, S.; Paine, T. K. Aliphatic C-C Bond Cleavage of α-Hydroxy Ketones by Non-Heme Iron(II) Complexes: Mechanistic Insight into the Reaction Catalyzed by 2,4'-Dihydroxyacetophenone Dioxygenase. *Inorg. Chem.* **2015**, *54*, 10576−10586.

(18) Siewert, L.; Limberg, C. A Trispyrazolylborato Iron Malonato Complex as a Functional Model for the Acetylacetone Dioxygenase. *Angew. Chem., Int. Ed.* **2008**, *47*, 7953−7956.

(19) Li, J.; Banerjee, A.; Pawlak, P. L.; Brennessel, W. W.; Chavez, F. A. Highest Recorded N-O Stretching Frequency for 6-Coordinate $\{\text{Fe-NO}\}^7$ Complexes: An Iron Nitrosyl Model for His_3 Active Sites. *Inorg. Chem.* **2014**, *53*, 5414−5416.

(20) Banerjee, A.; Li, J.; Speelman, A. L.; White, C. J.; Pawlak, P. L.; Brennessel, W. W.; Lehnert, N.; Chavez, F. A. A Structural Model for the Iron-Nitrosyl Adduct of Gentisate Dioxygenase. *Eur. J. Inorg. Chem.* **2018**, *2018*, 4797−4804.

(21) Li, J.; Banerjee, A.; Preston, D. R.; Shay, B. J.; Adhikary, A.; Sevilla, M. D.; Loloee, R.; Staples, R. J.; Chavez, F. A. Thermally Induced Oxidation of $[\text{Fe}^{\text{II}}(\text{tacn})_2](\text{OTf})_2$ (tacn = 1,4,7-triazacyclononane). *Eur. J. Inorg. Chem.* **2017**, *2017*, 5529−5535.

(22) Spek, A. L. PLATON, version 150216. *Acta Crystallogr., Sect. C: Struct. Chem.* **2015**, *71*, 9−18.

(23) Addison, A. W.; Rao, T. N.; Reedijk, J.; van Rijn, J.; Verschoor, G. C. Synthesis, Structure, and Spectroscopic Properties of Copper(II) Compounds Containing Nitrogen−Sulphur Donor Ligands; the Crystal and Molecular Structure of aqua[1,7-bis(*N*-methylbenzimidazol-2-yl) −2,6-dithiaheptane]-copper(II) perchlorate. *J. Chem. Soc., Dalton Trans.* **1984**, 1349−1356.

(24) Christie, S.; Wang, L. H.; Zaworotko, M. J. Ionic Liquid Mediated Synthesis and X-Ray Crystal Structure of *trans*-Difluorotetrakis-(1-methylimidazole)iron(III) Tetrafluoroborate. *Inorg. Chem.* **1993**, *32*, 5415−5417.

(25) Chauvin, A. S.; Frapart, Y. M.; Vaissermann, J.; Donnadieu, B.; Tuchagues, J. P.; Chottard, J. C.; Li, Y. Synthesis, X-ray Crystal Structure, and Redox and Electronic Properties of Iron(III)-Polyimidazole Complexes Relevant to the Metal Sites of Iron Proteins. *Inorg. Chem.* **2003**, *42*, 1895−1900.

(26) Marlin, D. S.; Olmstead, M. M.; Mascharak, P. K. Reaction of (μ-Oxo)diiron(III) Core with CO_2 in *N*-methylimidazole: Formation of Mono(μ-carboxylato)(μ-oxo)diiron(III) Complexes with *N*-Methylimidazole as ligands. *Inorg. Chem.* **2003**, *42*, 1681−1687.

(27) Sunatsuki, Y.; Ohta, H.; Kojima, M.; Ikuta, Y.; Goto, Y.; Matsumoto, N.; Iijima, S.; Akashi, H.; Kaizaki, S.; Dahan, F.; Tuchagues, J. P. Supramolecular Spin-Crossover Iron Complexes Based on Imidazole-Imidazolate Hydrogen Bonds. *Inorg. Chem.* **2004**, *43*, 4154−4171.

(28) Gorun, S. M.; Papaefthymiou, G. C.; Frankel, R. B.; Lippard, S. J. Synthesis, Structure, and Magnetic and Mossbauer Properties of Mononuclear and Asymmetric, Oxo-Bridged Trinuclear Iron(III) Complexes of a New Polyimidazole Ligand. *J. Am. Chem. Soc.* **1987**, *109*, 4244−4255.

(29) Smedarchina, Z.; Fernández-Ramos, A.; Siebrand, W. Tunneling Dynamics of Double Proton Transfer in Formic Acid and Benzoic Acid Dimers. *J. Chem. Phys.* **2005**, *122*, 134309.

(30) Mènage, S.; Que, L., Jr. (μ-Oxo) (μ-Carboxylato) Diiron(III) Complexes-Effects of the Terminal Ligands. *New J. Chem.* **1991**, *15*, 431−438.

(31) van der Donk, W. A.; Krebs, C.; Bollinger, J. M., Jr. Substrate Activation by Iron Superoxo Intermediates. *Curr. Opin. Struct. Biol.* **2010**, *20*, 673−683.

(32) Cicchillo, R. M.; Zhang, H.; Blodgett, J. A. V.; Whitteck, J. T.; Li, G.; Nair, S. k.; van der Donk, W. A.; Metcalf, W. W. An Unusual Carbon-Carbon Bond Cleavage Reaction During Phosphinothricin Biosynthesis. *Nature* **2009**, *459*, 871−874.

(33) Adam, W.; Matsumoto, M.; Trofimov, A. V. Viscosity Dependence of the Chemically Induced Electron-Exchange Chemiluminescence Triggered from a Bicyclic Dioxetane. *J. Am. Chem. Soc.* **2000**, *122*, 8631−8634.

(34) Adam, W.; Baader, W. J. Effects of Methylation on the Thermal Stability and Chemiluminescence Properties of 1,2-Dioxetanes. *J. Am. Chem. Soc.* **1985**, *107*, 410−416.

(35) Adam, W.; Baader, W. J. 1,2-Dioxetane: Synthesis, Characterization, Stability, and Chemiluminescence. *Angew. Chem., Int. Ed. Engl.* **1984**, *23*, 166−167.

(36) Adam, W.; Cueto, O. Fluorescer-Enhanced Chemiluminescence of α-Peroxylactones via Electron Exchange. *J. Am. Chem. Soc.* **1979**, *101*, 6511−6515.

(37) Hagen, K. S. Iron(II) Triflate Salts as Convenient Substitutes for Perchlorate Salts: Crystal Structures of $[\text{Fe}(\text{H}_2\text{O})_6](\text{CF}_3\text{SO}_3)_2$ and $\text{Fe}(\text{MeCN})_4(\text{CF}_3\text{SO}_3)_2$. *Inorg. Chem.* **2000**, *39*, 5867−5869.

(38) Frisch, M. J.; Trucks, G. W.; Schlegel, H. B.; Scuseria, G. E.; Robb, M. A.; Cheeseman, J. R.; Scalmani, G.; Barone, V.; Mennucci, B.; Petersson, G. A.; Nakatsuji, H.; Caricato, M.; Li, X.; Hratchian, H. P.; Izmaylov, A. F.; Bloino, J.; Zheng, G.; Sonnenberg, J. L.; Hada, M.; Ehara, M.; Toyota, K.; Fukuda, R.; Hasegawa, J.; Ishida, M.; Nakajima, T.; Honda, Y.; Kitao, O.; Nakai, H.; Vreven, T.; Montgomery, Jr., J. A.; Peralta, J. E.; Ogliaro, F.; Bearpark, M.; Heyd, J. J.; Brothers, E.; Kudin, K. N.; Staroverov, V. N.; Keith, T.; Kobayashi, R.; Normand, J.; Raghavachari, K.; Rendell, A.; Burant, J. C.; Iyengar, S. S.; Tomasi, J.; Cossi, M.; Rega, N.; Millam, J. M.; Klene, M.; Knox, J. E.; Cross, J. B.; Bakken, V.; Adamo, C.; Jaramillo, J.; Gomperts, R.; Stratmann, R. E.; Yazyev, O.; Austin, A. J.; Cammi, R.; Pomelli, C.; Ochterski, J. W.; Martin, R. L.; Morokuma, K.; Zakrzewski, V. G.; Voth, G. A.; Salvador, P.; Dannenberg, J. J.; Dapprich, S.; Daniels, A. D.; Farkas, O.; Foresman, J. B.; Ortiz, J. V.; Cioslowski, J.; Fox, D. J. *Gaussian09, Revision C.01*; Gaussian Inc., Wallingford CT, 2010.

(39) Petersson, G. A.; Al-Laham, M. A. A complete basis set model chemistry.II. Open-shell systems and the total energies of the first-row atoms. *J. Chem. Phys.* **1991**, *94*, 6081−6090.

(40) Hanwell, M.; Curtis, D.; Lonie, D.; Vandermeersch, T.; Zurek, E.; Hutchison, G. Avogadro: an advanced semantic chemical editor, visualization, and analysis platform. *J. Cheminf.* **2012**, *4*, 1−17.

(41) Neese, F.; Wennmohs, F.; Becker, U.; Riplinger, C. The ORCA quantum chemistry program package. *J. Chem. Phys.* **2020**, *152*, 224108.

(42) Lee, C.; Yang, W.; Parr, R. G. Development of the Colle-Salvetti correlation-energy formula into a functional of the electron density. *Phys. Rev. B: Condens. Matter Mater. Phys.* **1988**, *37*, 785−789.

(43) Becke, A. D. A new mixing of Hartree−Fock and local density-functional theories. *J. Chem. Phys.* **1993**, *98*, 1372−1377.

(44) Becke, A. D. Density-functional thermochemistry. III. The role of exact exchange. *J. Chem. Phys.* **1993**, *98*, 5648−5652.

(45) Schäfer, A.; Horn, H.; Ahlrichs, R. Fully optimized contracted Gaussian basis sets for atoms Li to Kr. *J. Chem. Phys.* **1992**, *97*, 2571−2577.

(46) Schäfer, A.; Huber, C.; Ahlrichs, R. Fully optimized contracted Gaussian basis sets of triple zeta valence quality for atoms Li to Kr. *J. Chem. Phys.* **1994**, *100*, 5829−5835.

(47) Petrenko, T.; Kossmann, S.; Neese, F. Efficient time-dependent density functional theory approximations for hybrid density functionals: Analytical gradients and parallelization. *J. Chem. Phys.* **2011**, *134*, No. 054116.

(48) Izsák, R.; Neese, F. An overlap fitted chain of spheres exchange method. *J. Chem. Phys.* **2011**, *135*, 144105.

(49) Barone, V.; Cossi, M. Quantum Calculation of Molecular Energies and Energy Gradients in Solution by a Conductor Solvent Model. *J. Phys. Chem. A* **1998**, *102*, 1995−2001.

(50) Zhurko, G. A.; Zhurko, D. A. *Chemcraft, Version 1.7* (Build 132).

(51) *APEX3, version 2017.3−0*; Bruker AXS: Madison, WI, 2017.

(52) Krause, L.; Herbst-Irmer, R.; Sheldrick, G. M.; Stalke, D. SADABS, version 2016/2. *J. Appl. Crystallogr.* **2015**, *48*, 3−10.

(53) *SAINT, version 8.34A*; Bruker AXS: Madison, WI, 2013.

(54) Sheldrick, G. M. SHELXT, version 2014/5. *Acta Crystallogr., Sect. A: Found. Adv.* **2015**, *71*, 3−8.

(55) Sheldrick, G. M. SHELXT, version 2017/1. *Acta Crystallogr., Sect. C: Struct. Chem.* **2015**, *71*, 3−8.

(56) *CrysAlisPro, version 171.39.43c*; Rigaku Corporation: Oxford, UK, 2018.

(57) Sheldrick, G. M. SHELXL, version 2018/1. *Acta Crystallogr., Sect. C: Struct. Chem.* **2015**, *71*, 3−8.